International Communications in Heat and Mass Transfer 158 (2024) 107962

Contents lists available at ScienceDirect

International Communications in Heat and Mass Transfer

journal homepage: www.elsevier.com/locate/ichmt

Optimal height distribution design and experimental validation of pin-fin heat sink under natural convection based on dynamic surrogate model

Wenhao Fan, Chunyu Shi, Wei Liu, Zhichun Liu *

School of Energy and Power Engineering, Huazhong University of Science and Technology, Wuhan 430074, China

ARTICLE INFO

Keywords:
Natural convection
Fin height distribution
Machine learning
Optimization
Numerical simulation

ABSTRACT

Pin-fin heat sinks are widely employed to dissipate heat from power devices under natural convection conditions. To improve heat dissipation performance, optimization of the fin height distribution was conducted in this study. In order to enhance optimization efficiency, we propose a dynamic surrogate model that integrates machine learning, iteratively sampling and training until the convergence criterion is met. Compared with traditional surrogate models, the dynamic surrogate model significantly reduces the prediction error of the optimal result, proving more efficient and yielding superior outcomes with fewer samples. By optimizing the fin height distribution, the heat sink thermal resistance was minimized without increasing mass. Subsequently, an experimental bench was developed to compare the heat sink's total thermal resistance pre- and post-optimization under natural convection conditions. Experimental results demonstrate that within the input heat flux range of q = 500–1200 W/m^2, the optimized heat sink's total thermal resistance is diminished by 6.08% to 8.01%, without any mass increment, which confirms the dynamic surrogate model's efficacy in natural convection scenarios. This study elucidates the design principles governing the height distribution of pin-fins of heat sinks under natural convection, and provides a significant insight for guiding the design of pin-fin heat sinks.

1. Introduction

For most power devices, maintaining the proper operating temperature range via effective thermal management is essential to ensure efficient operation [1–4]. In terms of thermal management, two primary heat transfer methods exist: active and passive, both aiming to remove undesirable heat [5]. Compared with active heat dissipation, passive methods do not require an external energy supply. Taking natural convection cooling as an example, this approach facilitates heat dissipation through thermal radiation and fluid convection resulting from buoyancy effects caused by temperature differences [6]. It is evident that passive heat dissipation technology is not only relatively environmentally friendly [7] but also boasts lower noise and smaller failure rates [3], albeit with a comparatively limited heat transfer capacity [8]. To enhance the heat transfer coefficient (HTC) of passive heat dissipation technology, optimizing the design of heat transfer elements is essential.

Convection heat sinks with fins are widely utilized in thermal management applications. Compared with forced convection, optimizing heat transfer in natural convection heat sinks proves more challenging due to their lower heat transfer intensity and the absence of a power source, necessitating a substantial reduction in convection resistance to enhance heat transfer performance [9–12]. Haghighi et al. [13] investigated the thermal performance of plate-fin and pin-fin heat sinks under natural convection and found that the latter exhibited lower thermal resistance, improving thermal performance by 10% to 41.6% compared with the former. Sertkaya et al. [14] also stated that, under conditions of natural convection, pin-fin heat sinks are not only lighter than plate-fin heat sinks but also enhance convective heat transfer. Consequently, the pin-fin heat sink was selected for the study to optimize the structure of the pin-fins with the objective of improving the natural convection heat dissipation performance.

Natural convection can be enhanced through three primary mechanisms: enhancing the convection coefficient, expanding the heat transfer surface area, and amplifying the temperature difference between the heat transfer medium and the surrounding environment. However, in practical applications, enhancing heat transfer proves to be much more complicated. Researchers have employed various optimization strategies to enhance the heat dissipation capabilities of heat sinks. In investigating innovative fin designs, Sung et al. [15] strengthened the chimney effect by affixing aluminum tape to a pin-fin heat sink, thereby

* Corresponding author.
E-mail address: zcliu@hust.edu.cn (Z. Liu).

https://doi.org/10.1016/j.icheatmasstransfer.2024.107962

Available online 19 August 2024

enhancing heat transfer and reducing thermal resistance by 17.1%. Kim et al. [16] conducted an experimental analysis on the thermal performance of heat sinks with branched pin-fins, discovering a 20% lower thermal resistance relative to the conventional pin-fin heat sink. Serkan Saahin et al. [17] examined flow and heat transfer characteristics of integrated pin fin-aluminum foam heat sinks, and analyzed various configurations to identify the relatively optimal design by numerical simulation. Sertkaya et al. [14] and Ahmadian-Elmi et al. [18] studied the effects of the size, shape, height, spacing of pin-fins, and placement angle of the heat sink on the heat dissipation ability under natural convection through numerical simulation and experiment. Researchers have also delved into non-uniform fin distribution designs; Bhandari et al. [19] examined the thermal performance of vertically-oriented pin-fin heat sinks with fin densities that varied along the flow direction under natural convection, revealing that heat sinks with fin densities decreasing along the flow direction exhibited an 11% reduction in thermal resistance and a 30% weight reduction when compared to heat sinks with uniformly distributed fins. Furthermore, studies by Huang et al. [10] and Jang et al. [11] demonstrated that heat sink's thermal resistance is lower when the height of the central area differs from that of the peripheral pin-fins. Baldry et al. [12] also observed that, with the central region's pin-fins at zero height, the temperature of the heat sink substrate was 1.1 K lower than that of a uniform height design.

The aforementioned studies indicate that, to enhance natural convection, numerous scholars utilize Computational Fluid Dynamics (CFD) simulations in conjunction with experiments to refine the heat sink structure. However, due to the inherent constraints of the test scope, considerable potential for optimization remains in the final design. Consequently, it is imperative to explore the pin-fin's optimal design using optimization algorithms to enhance both the thermal and hydraulic efficiencies of the heat sink [20–23]. Commonly utilized intelligent algorithms comprise the genetic algorithm (GA) [24–26], particle swarm optimization (PSO) [27], and simulated annealing (SA) [28]. The efficacy of these applications relies heavily on the reliability of the mathematical models that delineate the relationship between design variables and performance. Given the complexity of heat transfer optimization challenges and the constraints of computational resources, devising precise mathematical models for performance prediction constitutes a critical bottleneck in applying optimization algorithms. Surrogate models are mathematical formulations that approximate the relationship between input and output variables. Utilizing these surrogate models, resource-intensive CFD simulations can be substituted with rapid and cost-effective mathematical computations. Common surrogate models used in optimization include response surface models (RSM) [29], artificial neural network models (ANN) [30,31], Kriging model (KRG) [32], decision tree [33], and support vector regression models (SVR) [34]. Das et al. [35] applied Taguchi method and response surface methodology (RSM) for parametric optimization of natural convection heat transfer inside a triangular porous enclosure with in-line rectangular finned array to obtain the optimal combination of design parameters for maximum Nussle number. Shaeri et al. [36] devised a machine-learning-based model utilizing ANN and a greedy search algorithm to optimize the air-cooled plate-fin heat sink under laminar flow across a broad spectrum of design parameters. Gupta et al. [37] conducted a multi-objective optimization of an air-cooled perforated micro-pin-fin heat sink using an ANN surrogate model in tandem with the non-dominated sorting genetic algorithm (NSGA-II). Finally, the heat transfer performance was enhanced by 11.5% to 39.8%. Nguyen et al. [38] optimized the pin-fin geometry using a genetic algorithm integrated with machine learning and CFD simulation, resulting in a funnel-shaped design with a narrow top and wide base. Compared to conventional cylindrical pin-fins, the HTC of this heat sink increased by 20% without any detriment to hydraulic performance. In addition, recent years have seen the application of novel surrogate models in enhancing the performance of heat exchange equipment, such as convolutional neural networks (CNN) [39] and multimodal machine learning (MMML) [33]. Yang et al. [39] employed a pix2pix neural network, which consists of two adversarial CNN, to regress the thermal fluid information of pin-fin channels and used genetic algorithms for structural optimization of the fins.

The enhancement of optimization models contributes to improved prediction accuracy; however, the aforementioned models are all trained and generated based on a consistent dataset. This approach lacks the accuracy characteristics inherent to CFD simulations. Consequently, although these optimization methods boast high optimization efficiency and accuracy, their limitations become evident when confronted with the pronounced nonlinearity inherent in heat transfer optimization problems: (1)Due to the uncertainty regarding the location of the optimal design points, the majority of research endeavors prioritize global accuracy by employing uniform sampling. However, this sampling strategy results in sparse sampling around the optimal design points, inevitably compromising the fitting precision in these critical areas. This, in turn, leads to a discrepancy between the predicted and actual optimal designs. (2) During the construction of the traditional surrogate model, the absence of a uniform standard fails to clarify the necessary sample capacity needed for a specific optimization problem. In light of the aforementioned deficiencies, we plan to dynamically introduce additional sampling points in the vicinity of the optimal design points. This strategy aims to continuously refine the model's precision near these crucial areas while maintaining overall accuracy, thereby ensuring that the predicted optimal design converges ever closer to the actual optimal design. To improve the reliability of the optimization algorithm, Shi et al. [40–42] raised a dynamic surrogate model that marries the high computational precision of the CFD method with the rapid optimization capabilities of the traditional surrogate model.

Aiming to bolster natural convection and enhance the thermal performance of the heat sink, a dynamic agent model with constraints was developed in this study, which marries the high computational precision of the CFD calculations with the rapid optimization capabilities of the traditional surrogate model. The height distribution of pin-fins is optimized without increase in the mass of the heat sink. Through the analysis and comparison of gas velocity and heat sink surface temperature distributions before and after optimization, simulation results elucidated the mechanisms underlying the heat sink's enhanced performance. Subsequently, a test platform was established to evaluate the heat sink's heat dissipation efficiency under natural convection conditions, and the experimental results confirmed the dynamic surrogate model's efficacy in the realm of natural convection. The approach proposed herein equips engineers with a strategy to curtail superfluous time-intensive tasks and boost optimization efficiency.

2. Computational model and numerical method

2.1. Physical description of the problem

The structure of the pin-fin natural convection heat sink studied in this paper is shown in Fig. 1. The heat sink is placed horizontally and is composed of a substrate and pin-fins with a square section. The side length of the substrate is $2B = 120$ mm, the thickness is $t = 2$ mm, the side length of a single pin-fin is $d = 4$ mm, the initial height $H_0 = 50$ mm, and the number of pin-fins is $N = 100$. The transverse and longitudinal spacing between the fin is $s = 8$ mm, and the distance between the fin and the edge of the substrate is $d_a = 4$ mm. The heat source is attached to the bottom of the substrate, and the heat is finally dispersed into the air through fins. Due to structural symmetry, a quarter of the heat sink is selected as the calculation model. The calculation domain model is shown in Fig. 1 (d). The air domain is continuously expanded until the influence of the air domain boundary on the flow near the heat sink can be eliminated. Finally, the length, width, and height of the air domain can be determined as $2.5B \times 2.5B \times 6H_0$, respectively.

Natural convection has no power source and is only promoted by the buoyancy generated by the temperature difference. Therefore, the

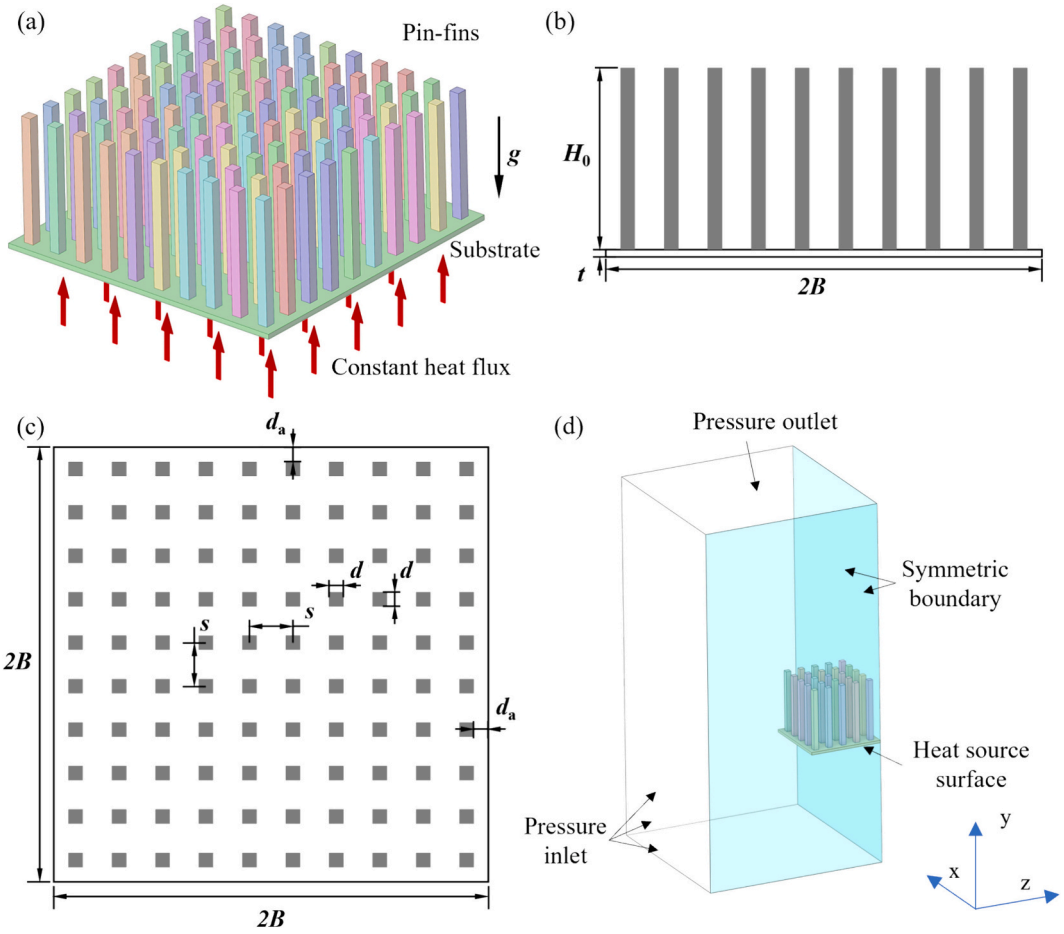

Fig. 1. Physical model and computational domain schematic of the pin fin heat sink: (a) three-dimensional view, (b) front view, (c) top view, and (d) computational domain and boundary conditions.

pressure inlet boundary is set around and on the bottom of the calculation domain, and the pressure outlet is on the top of the calculation domain, with atmospheric pressure $P_0 = 1.01325 \times 10^5$ Pa and ambient temperature $T_{amb} = 300$ K. On the solid side at the bottom of the heat sink, which serves as the heat source surface, an input heat flux of $q = 700$ W/m^2 is applied. The air side is designated as adiabatic, ensuring there is no heat loss from the back of the heat source. The remaining contact surfaces between the heat sink and the air constitute the fluid-solid interface.

2.2. Mathematical formulation and solution methods

By calculating Grashof number (*Gr*), natural convection in the calculation domain is steady-state laminar flow. Under the input power studied in this research, the temperature rise of the heat sink is small. The following reasonable assumptions can be used to simplify the governing equation:

(1) The physical properties except for density of the fluid domain are considered to be fixed;
(2) The solid domain material is uniformly isotropic, and the physical properties are also fixed;
(3) The acceleration of gravity is downward vertically along the negative Y-axis, and the value is $g = 9.8$ m^2/s;
(4) The pin-fins are molded integrally with the substrate ignoring contact thermal resistance.

For the fluid's density, *Boussinesq* approximation is adopted, that is, the density in the volume force term of the momentum equation is considered to change linearly. The calculation formula is as follows:

$$\rho = \rho_0\text{-}\beta_q \rho_0 \Delta T \tag{1}$$

where β_q is the coefficient of thermal expansion, ρ_0 is the density of air at ambient temperature (T_{amb}), and ΔT represents the difference between the actual air temperature and T_{amb}. All the densities of the remaining governing equations are considered to be constant, and the simplified control equations are as follow:

Fluid domain:

$$\rho_0\left(\frac{\partial u}{\partial x}+\frac{\partial v}{\partial y}+\frac{\partial w}{\partial z}\right)=0 \tag{2}$$

$$\rho_0\left(\frac{\partial(u^2)}{\partial x}+\frac{\partial(uv)}{\partial y}+\frac{\partial(uw)}{\partial z}\right)=-\frac{\partial P}{\partial x}+\mu\left(\frac{\partial^2 u}{\partial x^2}+\frac{\partial^2 u}{\partial y^2}+\frac{\partial^2 u}{\partial z^2}\right) \tag{3}$$

$$\rho_0\left(\frac{\partial(uv)}{\partial x}+\frac{\partial(v^2)}{\partial y}+\frac{\partial(vw)}{\partial z}\right)=-\frac{\partial P}{\partial y}+\mu\left(\frac{\partial^2 v}{\partial x^2}+\frac{\partial^2 v}{\partial y^2}+\frac{\partial^2 v}{\partial z^2}\right)+g(\rho-\rho_0) \tag{4}$$

$$\rho_0\left(\frac{\partial(uw)}{\partial x}+\frac{\partial(wv)}{\partial y}+\frac{\partial(w^2)}{\partial z}\right)=-\frac{\partial P}{\partial z}+\mu\left(\frac{\partial^2 w}{\partial x^2}+\frac{\partial^2 w}{\partial y^2}+\frac{\partial^2 w}{\partial z^2}\right) \tag{5}$$

$$\rho_0\left(\frac{\partial(uT)}{\partial x}+\frac{\partial(vT)}{\partial y}+\frac{\partial(wT)}{\partial z}\right)=\frac{k}{c_p}\left(\frac{\partial^2 T}{\partial x^2}+\frac{\partial^2 T}{\partial y^2}+\frac{\partial^2 T}{\partial z^2}\right) \tag{6}$$

where *u*, *v*, and *w* represent the components of the gas velocity in the x,

y, and z directions, respectively; P denotes the local pressure; T indicates the local temperature; and μ, k and c_p are the viscosity, thermal conductivity, and specific heat at constant pressure of the gas, respectively.

Solid domains:

$$\frac{\partial^2 T}{\partial x^2}+\frac{\partial^2 T}{\partial y^2}+\frac{\partial^2 T}{\partial z^2}=0 \tag{7}$$

The numerical computation in this study utilizes the ANSYS Fluent, and employs the finite volume method to discretize and solve the computational domain. The radiation model is based on Surface to Surface model (S2S), and the momentum term as well as the energy term are discretized using a second order upwind approach. The pressure-velocity coupling is performed using the SIMPLE algorithm. The convergence criteria have been set at 10^{-6} for the continuity and velocity residuals, and 10^{-8} for the energy residuals.

The input power Q_{in} and heating surface temperature distribution can be obtained by numerical simulation methods or experimental measurements. Based on the average temperature of the heat source surface T_h, the total thermal resistance R_h of the heat sink can be calculated as:

$$R_h=\frac{T_h-T_{amb}}{Q_{in}} \tag{8}$$

2.3. Grid independence and model validation

In this study, a hexahedral structured mesh is used to partition the computational domain, with the mesh schematic diagram depicted in Fig. 2. The mesh is appropriately encrypted in the region of large velocity and temperature gradients near the contact surface between the fluid domain and the solid domain. A non-isometric structure is randomly generated to control the number of structural mesh nodes to generate different numbers of mesh systems. The total thermal resistance of the pin-fin is used as an index to verify the mesh independence, with the results shown in Table 1. It is found that when the mesh exceeds 4.36 million, the average change in total thermal resistance is no >1%. Hence it can be considered that the mesh system with 4.36 million mesh satisfies the calculation requirements.

Elenbaas [43] investigated the natural convection in a vertical channel between isothermal flat plates and obtained an empirical correlation for natural convection at a spacing of s and a height of H, as shown in Eq. (9). In order to avoid the prediction error associated with Eq. (9) when the value of s/H tends to 0, Bar-Cohen and Rohsenow [44] further obtained an empirical equation with a wider range of applicability, such as Eq. (10), where $C_1 = 576$ and $C_2 = 5.87$. In order to validate the correctness of the simulation of natural convection, numerical simulations of the natural convection in the vertical channel were established, and the results obtained are compared with the two empirical equations, as shown in Fig. 3. The comparison shows that the error between the results from numerical simulation and empirical correlations is small, which proves that the simulation method is reliable.

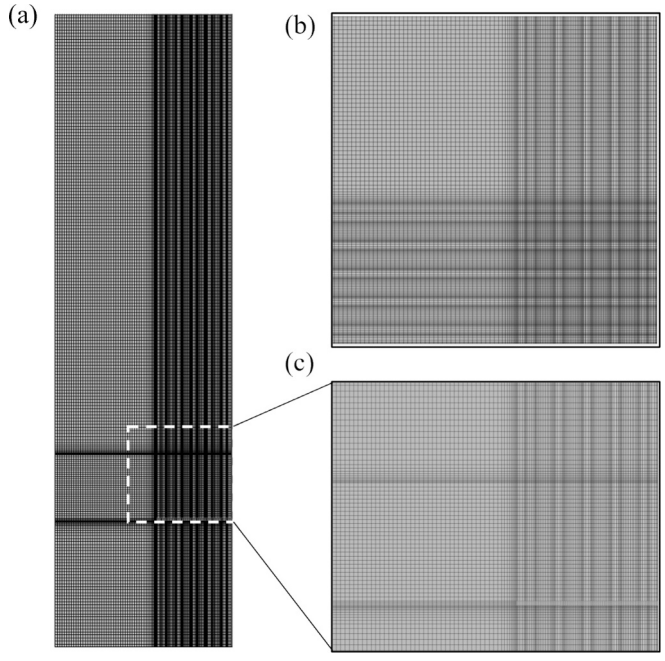

Fig. 2. Computational domain grid: (a) front view, (b) top view, and (c) local mesh view.

Table 1
Grid Independence Test.

Number of grids	Total thermal resistance	Inaccuracy
1,529,481	1.6369	–
4,367,481	1.6101	1.637%
7,198,521	1.6079	0.137%

$$Nu_s=\frac{1}{24}Ra_s\left(\frac{s}{H}\right)\left\{1-exp\left[-\frac{35}{Ra_s(s/H)}\right]\right\}^{3/4} \tag{9}$$

$$Nu_s=\left[\frac{C_1}{(Ra_s s/H)^2}+\frac{C_2}{(Ra_s s/H)^{1/2}}\right]^{-1/2} \tag{10}$$

where Nu and Ra represent the Nusselt number and Rayleigh number, respectively, and the subscript 's' denotes the solid phase.

3. Optimization method and procedure

3.1. The optimization problem description

This research focuses on how the height distribution of the pin-fins impacts the heat transfer performance of a natural convection heat sink. In the numerical model, pin-fin height values are organized into a height matrix, as depicted in Fig. 4. Given the symmetrical arrangement of the pin-fins, the optimization algorithm asserts that $h_{ij} = h_{ji}$, thereby reducing the height matrix to an upper triangular matrix comprising fifteen elements. These elements serve as design variables in the pursuit of optimizing the natural convection total thermal resistance. The pursuit of a lightweight design is a longstanding objective in the

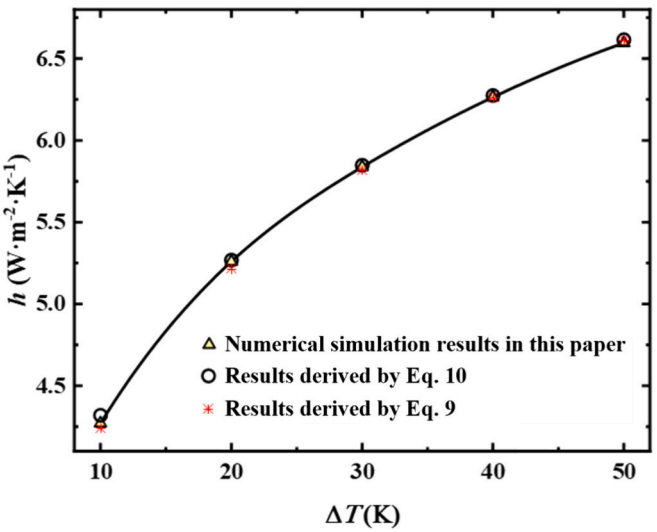

Fig. 3. Comparison of experimental and simulation results.

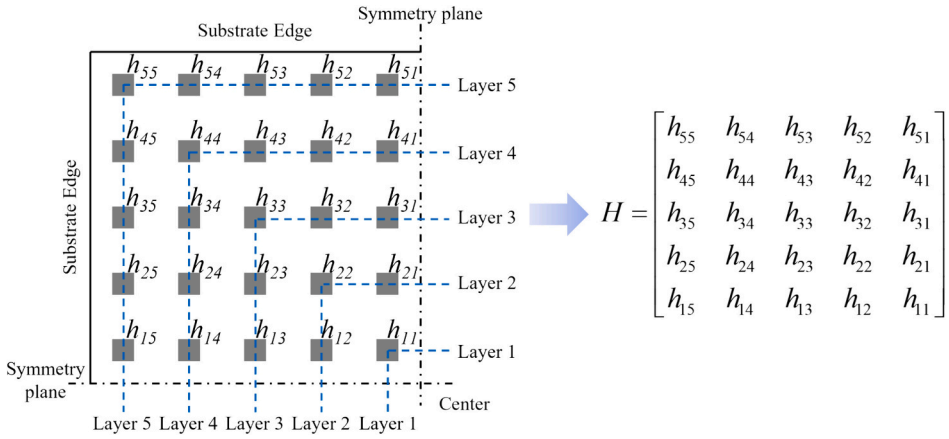

Fig. 4. Height matrix representing the pin-fin height distribution.

development of natural convection heat sinks. Consequently, to facilitate a meaningful comparison, this study imposes a constraint on the total mass of the heat sink, overseeing that the optimal heat transfer performance is achieved without surpassing the initial design's weight. With all other structural parameters held constant, the height of the pin-fins is singled out as the sole design variable. Thus, framing the optimization challenge addressed in this research as follows:

Optimization objective: $J = R_h$;

Design variables: h_{ij} ($i, j = 1, 2, \ldots, 5$);

Variables range: $h_{ij} \in [20, 80]$;

Constraints: $\Delta M = M_{ini} - M \geq 0$;

where M_{ini} is the total mass of the initial isometric pin-fin heat sink, $M_{ini} = 25\rho_s \times H_0 \times d_a^2 + \rho_s \times (2B)^2 \times t$. And ρ_s presents solid density.

3.2. Dynamic surrogate model under constraints

Dynamic surrogate model provides a strategy to guide the surrogate model to optimize an unknown black-box function effectively. It operates according to a two-step process: Initially, the surrogate is constructed using a small select group of sample points, followed by iterative updates through machine learning until the best value is no longer improved. Compared with a traditional surrogate model, the dynamic surrogate model can obtain the desired result with fewer samples and enhance the optimization efficiency. Moreover, continuous exploration can assist in identifying neglected local features and minimizing the influence of prediction errors on optimization results. The study by Shi et al. [41] has comprehensively validated the feasibility, efficiency, and accuracy of this method; hence, this aspect will not be

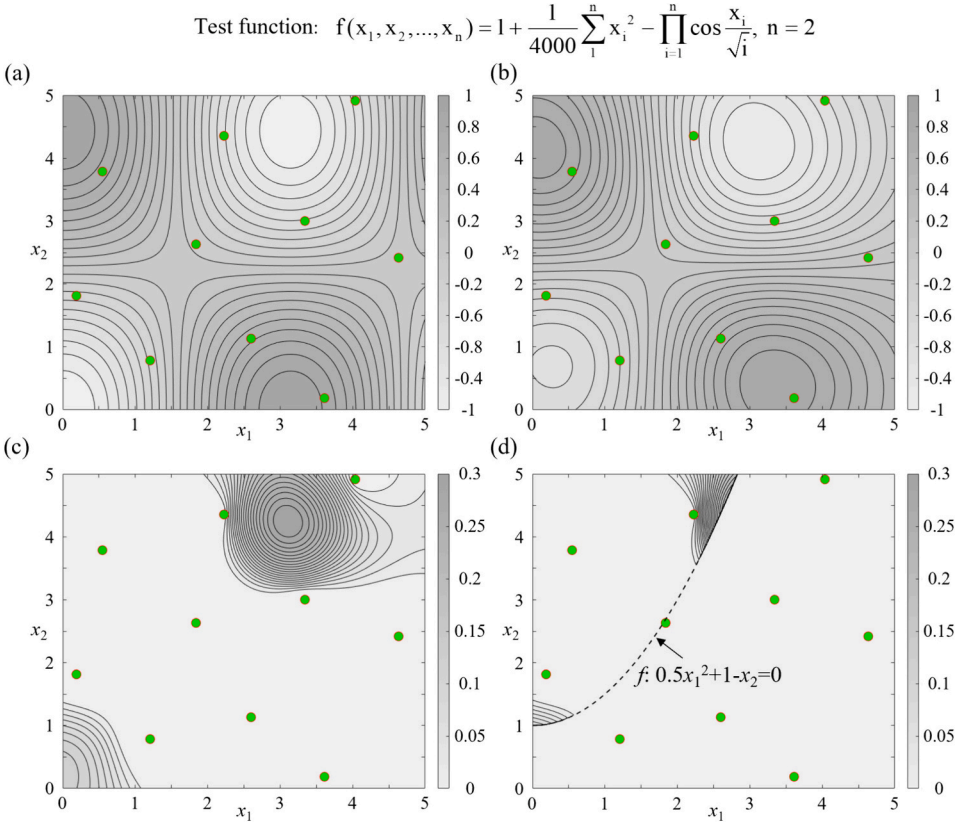

Fig. 5. Schematic of the constrained dynamic surrogate model: (a) example function distribution, (b) Kriging model fit distribution, (c) *EI* distribution without constraints, and (d) *EI* distribution with constraints.

reiterated in the present study.

In this study, Latin hypercube sampling (LHS) serves as the sampling design method; the Kriging model (KRG) has been chosen as the surrogate model, and a genetic algorithm is utilized to identify the optimal value. In the process of updating, newly-added sample points tend to converge around the optimal value. When confronted with constrained optimization problems, if the optimal value resides outside the constraint space, numerous selected candidate sample points become ineffective. Consequently, it is imperative to adjust the expected improvement (*EI*) values of the surrogate model to guarantee that the integrated sample points fall within the constraint space, thereby securing the optimal solution within the constraint space. Here we choose the Griewank function as an example to show this constraint imposition method. Its distribution in a two-dimensional plane is shown in Fig. 5 (a), where the shading indicates the function's value, and the closed curves represent the function's contour lines. The LHS method was employed for sampling, and the KRG model was utilized for assessment, yielding the predictive distribution function illustrated in Fig. 5 (b). This is derived from multiple data points in Fig. 5 (a), but due to data incompleteness and the complexity of the example function, there are some differences between the function images in Fig. 5 (a) and (b). Using the KRG model, we can also obtain the *EI* values in the two-dimensional plane as shown in Fig. 5 (c). The value of *EI* considers the Gaussian distribution of the test point positions and the current model's optimal value, representing the expected value of test points being lower than the current model's minimum value. In other words, a higher *EI* value indicates a higher likelihood of being the optimal design point, and the location with the maximum *EI* will be selected as the position for the candidate sample point by balancing the standard normal cumulative distribution function and the standard normal probability density function. The specific calculation method can be found in reference [41]. This method not only considers the current optimal value but also the distribution of errors. From an expectation perspective, the distribution of *EI* values takes into account both the probability of improving the current predicted function's minimum value and the extent of the improvement, thereby greatly enhancing optimization efficiency. From Fig. 5 (c), we can see that without constraints, the location of EI_{max} is at the center of multiple rings in the upper right corner. After applying constraints, the penalty function sets the *EI* values in the non-compliant regions to zero, resulting in the new *EI* distribution shown in Fig. 5 (d). It can be seen that the location of EI_{max} satisfying the constraints differs from the original, meaning the candidate point changes. This ensures that the progressively included sample points remain within the constrained space, aiding in finding the optimal solution within the constrained space.

The detailed methodology is depicted in Fig. 6. In this study, we initially conduct uniform sampling of the initial sample set with a size $N_i = 150$. The initial sample points are evaluated to determine their compliance with the constraints, and those failing to meet the constraints are excluded, resulting in a subset, S_{con}, comprising $N_{i,\ con} = 79$ sample points. The sample points in S_{con} are then assessed to establish initial performance metrics, leading to the formulation of the initial surrogate model distribution. Integrating the distribution with a genetic algorithm to refine the surrogate model, yielding a primordial minimal thermal resistance value of $R_h = 1.635$ K/W. With ongoing optimization, the total thermal resistance of the heat sink progressively declined, and ultimately, at $N_a = 270$, with EI_{max} falling below 10^{-4}, the process culminated in the attainment of a constrained minimum thermal resistance value of $R_h = 1.495$ K/W, as depicted in Fig. 7. Examination of the constrained (M_{ini} -*M*) values reveals that the masses of newly added sample points remain below that of the initial heat sink, indicative of consistent adherence to the constraints throughout the optimization. Subsequent iterations maintained a minimal discrepancy between the mass of the original heat sink and that of the new sample points, suggesting that within the imposed constraints, optimal thermal performance of the heat sink is achieved when its mass approaches its upper

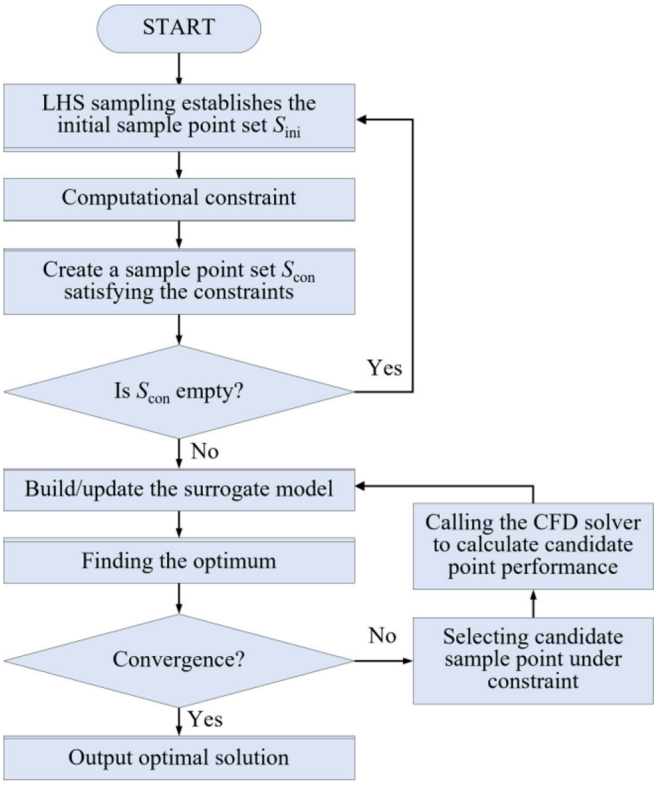

Fig. 6. Dynamic surrogate model optimization flow under constraints.

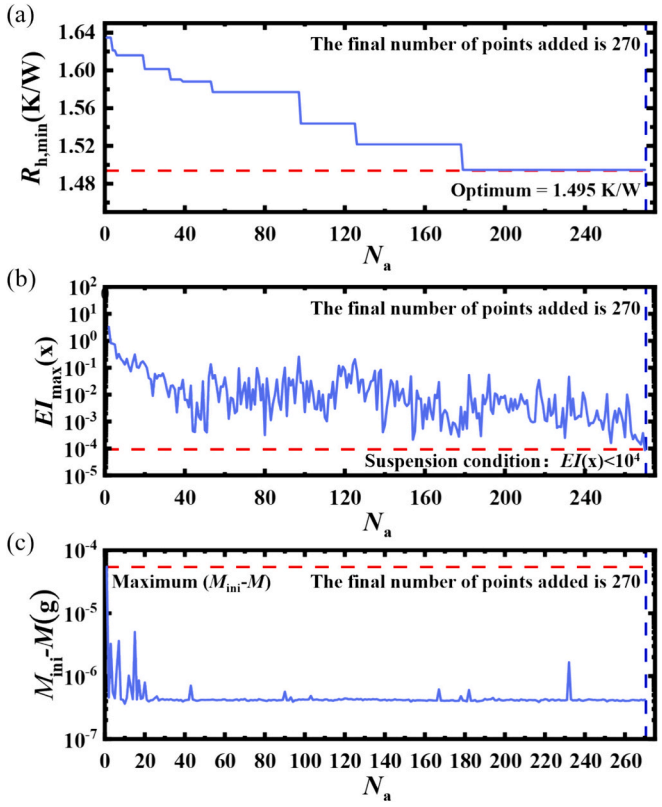

Fig. 7. Optimization process: (a) minimum thermal resistance, $R_{h,\ min}$, varies with N_a, (b) maximum EI_{max} varies with N_a, and (c) maximum ($M_{ini} - M$) varies with N_a.

limit.

4. Optimization results and discussion

The optimized height distribution for the best natural convection performance of the pin-fin heat sink are shown in Fig. 8. The figure illustrates a concave distribution pattern, with lower heights in the central region and increasing heights towards the periphery of the heat sink's pin-fins. Excluding h_{31} and h_{13}, the pin-fin heights within the inner three layers are designated as the lowest in the design spectrum. Conversely, the outermost pin-fins, with the exception of the diagonal fin h_{55}, assume the maximal values permitted by the design parameters. The fourth layer of pin-fins is distributed in a high/low cross pattern. Throughout the optimization, the height distribution of the pin-fins underwent significant alteration without increased mass. This indicates that uniform pin-fin heights do not facilitate optimal heat dissipation, and that a varied height profile, with taller pin-fins at the periphery and shorter ones internally, enhances thermal management.

Upon stabilization of the heat transfer between the heat sink and ambient air following an internal heat flow input, the surface temperature distribution is depicted in Fig. 9. In the original design, the substrate's overall temperature is elevated owing to heat influx, with the peak temperature reaching 316.88 K at the center. Heat entering the pin-fins disperses via natural air convection from the surface outward, resulting in a temperature gradient decreasing upwards. Influenced by solid thermal conductivity and natural air convection intensities, varying average temperatures are observed in the pin-fins at different locations, primarily evidenced by higher temperatures in the central area and lower temperatures in the peripheral regions. However, following pin-fin height optimization, the heat sink's surface temperature is notably reduced, with the central maximum temperature diminishing to 315.97 K—a decrease of 0.91 K from the pre-optimization state. Pin-fins at the heat sink's edge exhibit the most substantial temperature decline, attributed to the more intense natural convection and their extended length.

Heat dissipation of various pin-fins is depicted in Fig. 10. Alterations in the heights of pin-fins on a uniform substrate, while not affecting the overall heat dissipation area, result in a redistribution of thermal dissipation across the fins. Prior to optimization, a uniform height distribution resulted in more efficacious natural convection heat transfer in the peripheral pin-fins and less effective internal natural convection, leading to greater heat dissipation in the outer regions and reduced dissipation centrally. Within the same layer, the pin-fin located diagonally exhibits the lowest heat dissipation, which incrementally increases towards both ends of the diagonal. Post-optimization, the diminished heat dissipation area of the central pin-fin induces a rise in its local thermal resistance, whereas the heightened peripheral pin-fins experience decreased local thermal resistance, cumulatively decreasing the heat sink's overall thermal resistance due to the internal and peripheral modifications. Concurrently, the external pin-fins in direct contact with cool air expedite direct heat removal by the ambient air, thereby diminishing the internal pin-fins' heat dissipation requirements and consequently lowering the post-optimization temperature increment of the heat sink.

Fig. 11 and Fig. 12 illustrate the velocity and temperature distribution in cross-sectional views of heat sinks at varied heights, where sections A, B, C, and D correspond to elevations at $y = 20$, 40, 60, and 80 mm, respectively, and section E is the symmetric boundary of the XY plane. As depicted in the figures, the heat sink facilitates heat transfer from the pin-fins to the internal air; the air density decreases upon heating, and the generated negative pressure induces a suction force, driving cold external air flow horizontally towards the interior of the heat sink. The viscous resistance exerted by the pin-fins' surfaces upon the air diminishes the horizontal velocity component; concurrently, gravity induces an upward buoyant force, creating a vertical flow ascending through the channels between the pin-fins. The peripheral pin-fins of the heat sink, being in direct contact with the ambient cold air, experience an incomplete boundary layer development, culminating in a higher heat transfer intensity. During the inward airflow, the temperature boundary layer around each pin-fin fully develops and merges with the boundary layers of adjacent fins, leading to a lower heat transfer intensity within the inner pin-fins.

Prior to the optimization of uniform-height pin-fins, sections A and B exhibit identical pin-fin distributions; the difference in fluid and wall viscous resistance is negligible, resulting in a buoyancy-driven increase in airflow velocity from section A to section B. Transitioning from section B to sections C and D, where pin-fins are absent, the internal airflow of the heat sink encounters negligible viscous resistance. The external cold air streams directly flow above the heat sink, converging with the fluid emanating from the heat sink, thereby forming a vertical updraft. With respect to temperature distribution, as air enters the heat sink and is continuously heated by the pin-fins, its temperature progressively increases, culminating in a significant temperature elevation in the heat sink's central zone. In sections C and D, the direct intermingling of cooler external fluid with the warmer internal fluid markedly diminishes the extent of the high-temperature zone. Owing to the absence of a heating source, the high-temperature zone progressively contracts vertically.

Comparing the gas velocity distribution results of sections C and D before and after optimization, it is evident that the maximum gas velocity above the heat sink is higher post-optimization, with a larger high-velocity area. Analyzing the gas velocity distribution of section E before and after optimization reveals that the inward flow speed of the gas within approximately 70 mm above the heat sink substrate significantly increases post-optimization. This indicates that the optimized pin-fin structure has notably enhanced the intake of external gas.

Upon optimizing the heat sink's height, the reduced height of the

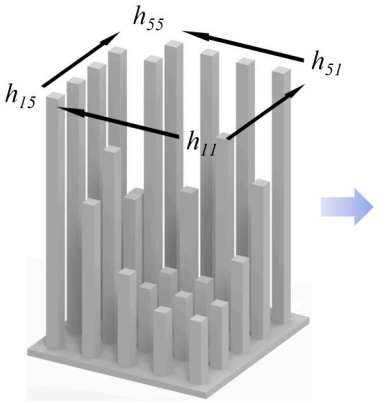

$$H = \begin{bmatrix} 30.021 & 80 & 80 & 80 & 80 \\ 80 & 80 & 40.965 & 60.888 & 48.838 \\ 80 & 40.965 & 20 & 20 & 29.299 \\ 80 & 60.888 & 20 & 20 & 20 \\ 80 & 48.838 & 29.299 & 20 & 20 \end{bmatrix}$$

Fig. 8. Matrix of optimal heights for pin-fin heat sinks.

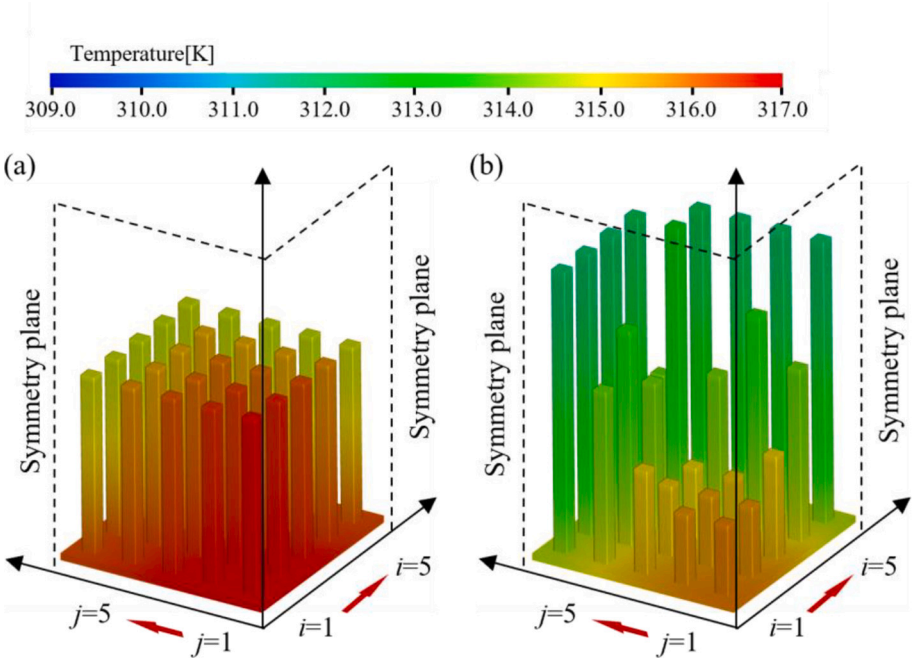

Fig. 9. Heat sink temperature distribution: (a) pre-optimization and (b) post-optimization.

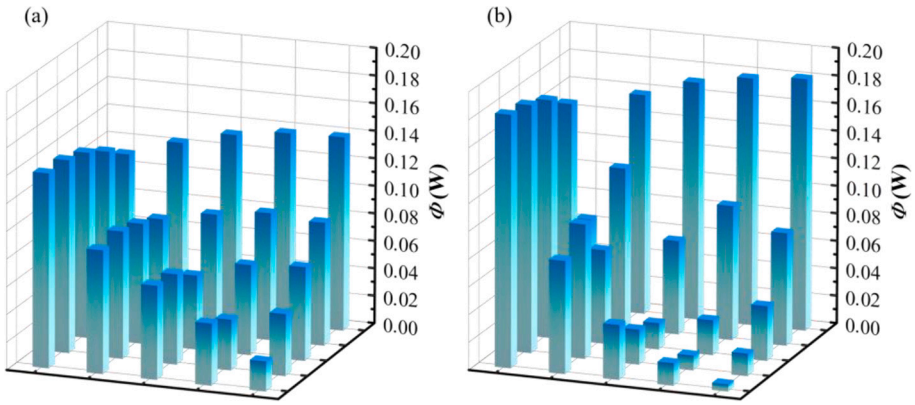

Fig. 10. Heat dissipation of each pin-fin: (a) pre-optimization and (b) post-optimization.

pin-fins in the central region diminishes the heat imparted to the air in this region, decelerating the increase in air temperature and consequently leading to a more homogeneous temperature distribution within the cross-section. Concurrently, the reduction in pin-fin height diminishes the fluid resistance within the heat sink, accelerating air entry, extending the development of the temperature boundary layer, and consequently enhancing the natural convection heat transfer capacity of the heat sink. In Sections C and D, the peripheral pin-fins remain in direct contact with the cold air; despite heat being transferred to the air via these fins, the gas within the central region is still hotter. The cooler peripheral gas is drawn towards the central region by suction, which reduces the central region's gas temperature.

The comparison of air mass flow rate and average temperature across the x-z section for various vertical y-values pre- and post-optimization is depicted in Fig. 13. At $y = 10$ mm, the contraction of the high-temperature zone results in the average temperature of the optimized structure being 1.145 K lower than its pre-optimization counterpart. As the y-coordinate increases, the air within the pre-optimization section absorbs more heat. Vertically, the thickening of the natural convection temperature boundary layer results in diminishing heat transfer intensity, and a consequent rise in the section's average temperature. Beyond $y = 50$ mm, where the pin-fins cease, external cold air flows above the heat sink, mixing with the high-temperature fluid and thereby reducing the section's average temperature. Post-optimization, with the minimal pin-fin height set at 20 mm, a slight increase in air temperature heated by the pin-fins is observed within the $y = 10$–20 mm range. Subsequently, the persistent influx of cold air leads to the mixing of cooler external air with the heated internal air of the heat sink, culminating in a gradual reduction of the fluid temperature. Ultimately, the lowest average temperature is recorded at section $y = 80$ mm. The change in mass flow rate indicates its increasing with height. Following the optimization of the fin height, there is a reduction in the heat sink's internal flow resistance and a consistently higher air mass flow rate than prior to optimization, suggesting enhanced entry of cold air and superior heat dissipation performance of the heat sink.

To verify the effectiveness of the optimization, a comparison is drawn between the optimized "low center - high surround" structure and the "high center - low surround" design. To maintain equivalent quality between both designs, the height for the latter configuration is determined using the formula $H_c = 2H_0\text{-}H$, as depicted in Fig. 14. Comparative analyses of the optimal design and the "high center - low surround" design in terms of temperature and velocity are illustrated in Fig. 15 and

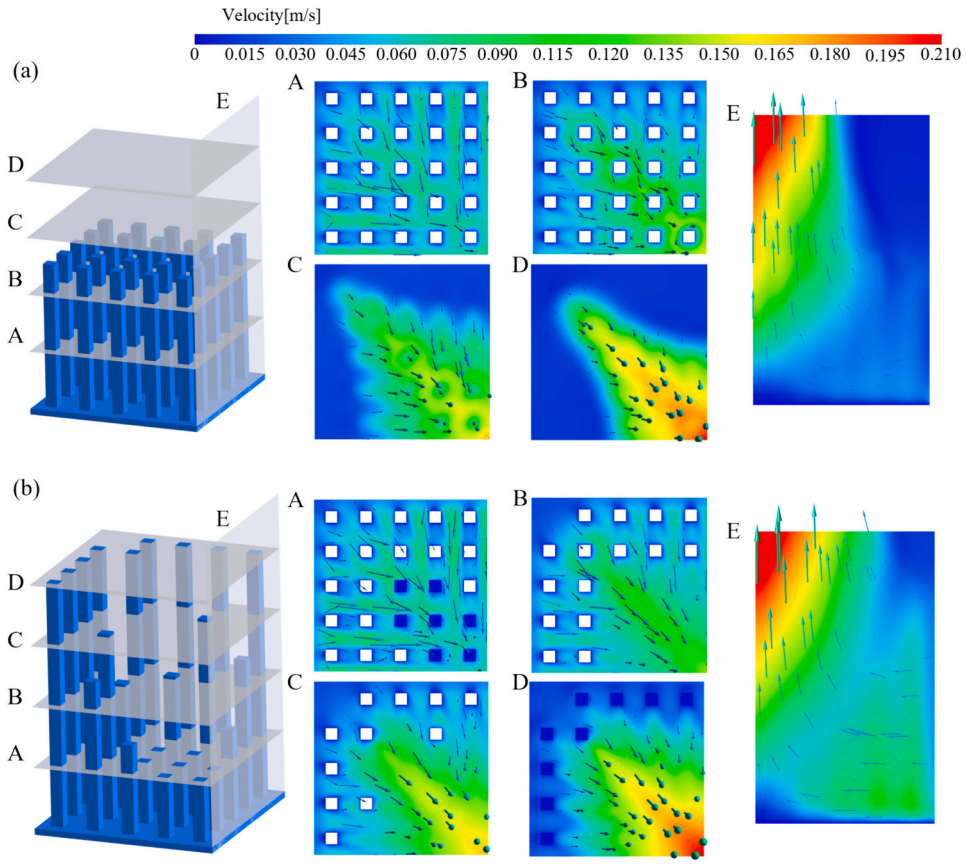

Fig. 11. Velocity distribution cloud for different cross sections: (a) pre-optimization and (b) post-optimization.

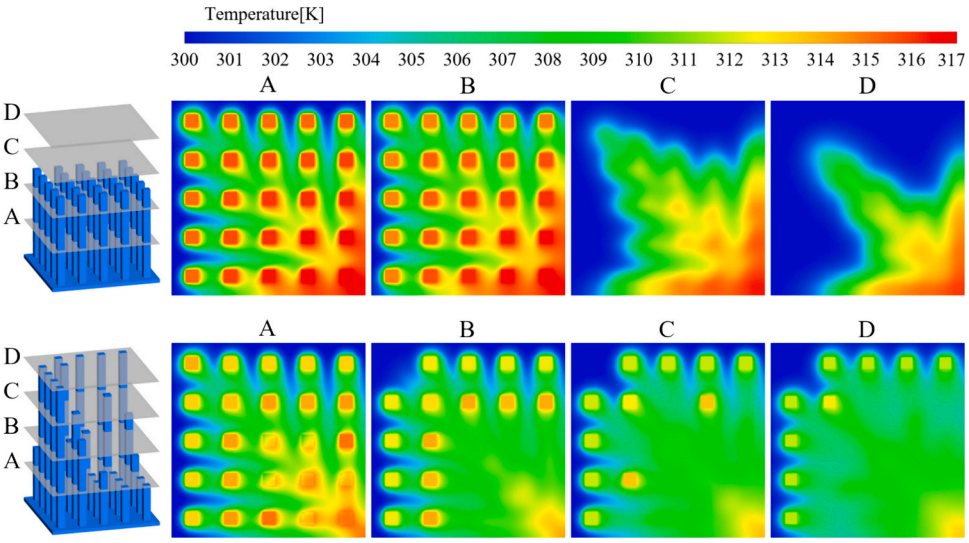

Fig. 12. Temperature distribution cloud map of different sections: (a) pre-optimization and (b) post-optimization.

Fig. 16, respectively. The diminished height of the peripheral pin-fins results in a weakened suction effect on the nearby air, leading to a decrease in the influx of cooler air into the heat sink, thereby hindering effective heat dispersion. Consequently, this results in a more extensive high-temperature zone at the design's center in the "high center - low surround" configuration, and an average heat sink temperature that exceeds the optimally designed average.

5. Experiment and verification

5.1. Experimental bench and procedure

An experimental bench has been constructed to conduct research on the optimization outcomes and to validate the performance of the enhanced heat sink. Fig. 17 and Fig. 18 depict the schematic and physical diagrams of the experimental bench, respectively. Placed horizontally on the bench, the heat sink interfaces with a polyimide heating

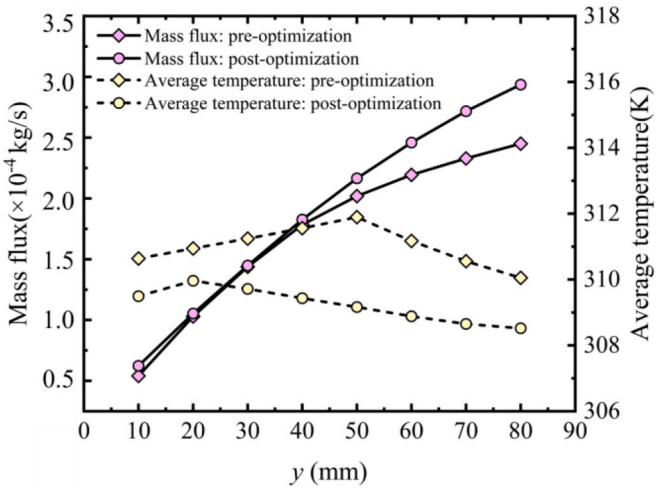

Fig. 13. Mass flux and average temperature of air in x-z section under different y values.

film, which matches the bottom shape of the substrate, serving as the experimental heat source. The heating wires within are tightly and uniformly arranged, ensuring a uniform heat flow throughout the heating process. A double layer of insulating cotton, with a thickness of 50 mm and a measured thermal conductivity of 0.034 W/(m·K), lines the back of the heating film to prevent experimental heat leakage into the air. An adjustable transformer, linked to a power meter with a 0.01 W rating, supplies the heating film's heat. T-type thermocouples are utilized, interfaced with the data acquisition system. To minimize thermocouple measurement error, nine temperature points between 293 K and 333 K are established, with a post-calibration error margin of ±0.1 K. Thirteen thermocouples are evenly distributed across the heating surface to gauge its average temperature, while an additional thermocouple monitors the ambient conditions. The thermocouples' distribution on the heating surface is illustrated in Fig. 19.

Additive manufacturing technology facilitates the processing of both the initial and the optimized models, yielding actual heat sinks that mirror the dimensions of the numerical prototypes. The aluminum alloy AlSi10Mg is employed as the material, possessing a density (ρ) of 2.665 g/cm^3, thermal conductivity (λ) of 147 W/(m·K), and specific heat capacity (c_p) of 890 J/(kg·K). The model surface is coated with TASCO blackbody spray to achieve an emissivity of approximately 0.94, with a temperature resistance up to 773 K. An electronic weighing measured the mass of pre- and post-optimization heat sinks. Fig. 18 (b) and Fig. 18 (c) display the heat sinks alongside the weighing results. Due to the manufacturing error, the pre-optimization heat sink weighing 290.0 g and the post-optimization heat sink is 289.7 g. The negligible mass difference of 0.3 g is <0.2% of the total mass, and permits the

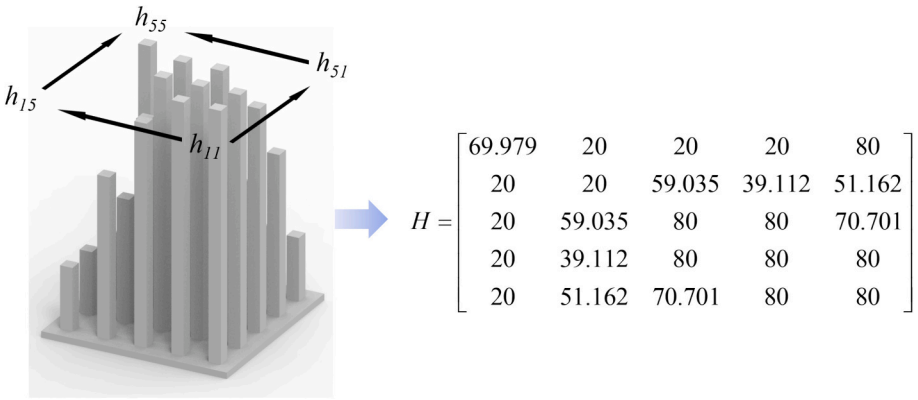

Fig. 14. "High center - low surround" heat sink structure design.

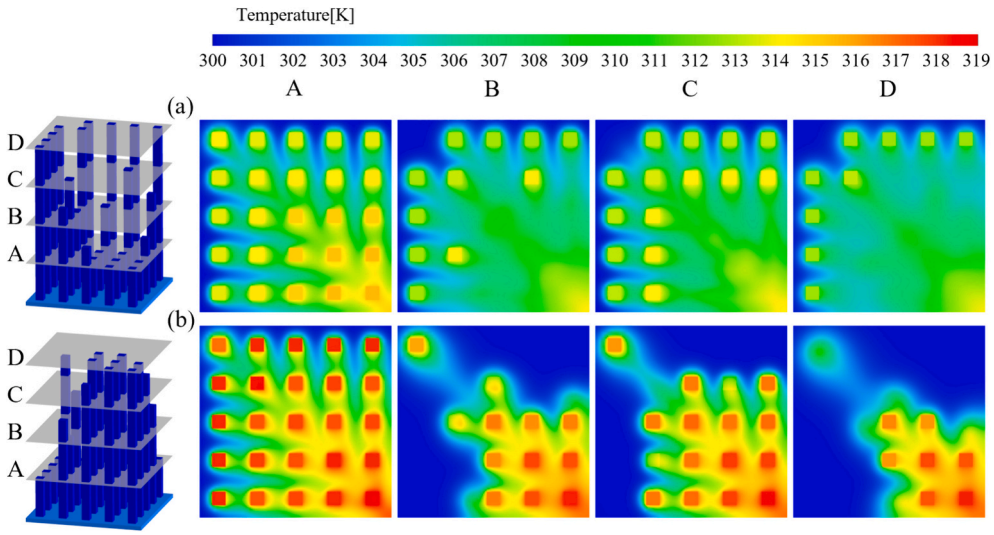

Fig. 15. Comparison of temperature distribution between optimal design and " high center - low surround" design: (a) optimal design and (b) "high center - low surround" design.

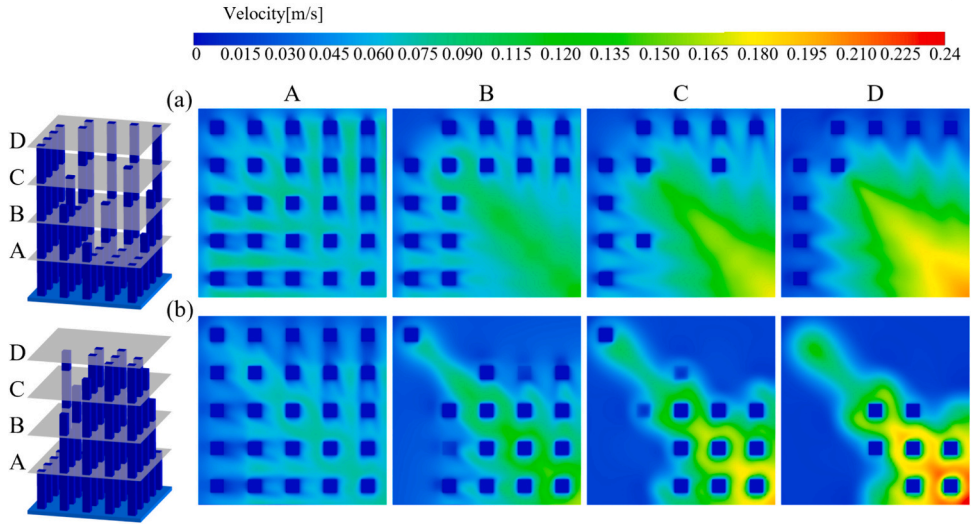

Fig. 16. Comparison of velocity distribution between optimal design and " high center - low surround " design: (a) optimal design and (b) "high center - low surround "design.

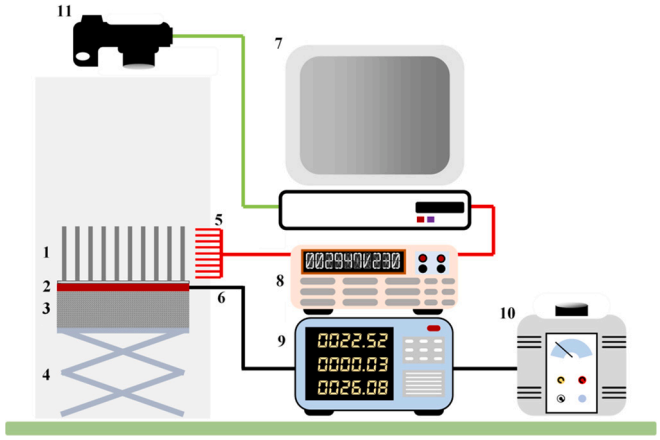

Fig. 17. Schematic diagram of the experimental bench: 1. Test heat sink; 2. Heating film; 3. Thermal insulation cotton; 4. Heat sink support rack; 5. Thermocouple; 6. Power input line; 7. Computer; 8. Data acquisition instrument; 9. Power meter; 10. Voltage regulator; 11. Infrared thermal imager.

assumption that their qualities are equivalent, thus considering the mass of the two heat sinks as identical.

Temperature distribution across the heat sink surface is gauged using an infrared thermal imager. The infrared imager, supplied by Fotric, boasts a measurement range from −233 K to 773 K. A fixed distance of 0.5 m is maintained between the infrared detector and the target, with ambient conditions recorded at 300 K and 70% humidity. Emissivity calibration of the coating is achieved by comparing thermocouple readings with infrared measurements at varying temperatures, ensuring the temperature discrepancy did not surpass ±0.2 K.

Upon construction of the experimental bench, environmental conditions are meticulously monitored and regulated to maintain a stable indoor temperature approximating 300 K, akin to the predetermined simulated conditions. This ensured minimal indoor air convection and negated interference from extraneous heat sources in proximity to the experimental setup. Ensuring no power leakage occurs, the power switch and data acquisition system are activated, followed by adjustment of the power supply to commence the experiment. The temperature at all measurement points is continuously observed. Once the temperature at all measurement points is stabilized, exhibiting fluctuations not exceeding 0.1 K over 20 min, the infrared camera is deployed to capture the heat sink's surface temperature.

5.2. Uncertainty analysis

Uncertainty analysis entails the estimation of experimental result errors attributable to the intrinsic measurement accuracy of the instrument used, constituting a crucial assessment of the experimental outcomes' reliability. For an assumed target value M, derived from several independent variables x_1, x_2, ….x_n that are uncorrelated, the associated experimental uncertainty is calculated using the formula below:

$$M = f(x_1, x_2, \ldots, x_n) \tag{11}$$

$$U(M) = \sqrt{\sum_{i=1}^{n} \left[\frac{\partial f}{\partial x_i} U(x_i)\right]^2} \tag{12}$$

The uncertainties $U(x_i)$ of the independent variables x_1, x_2, …, x_n are individually estimated to determine the total experimental measurement uncertainty. The total thermal resistance calculation is dependent on the heating surface temperature (T_h), the ambient temperature (T_{amb}), and the input power (Q_{in}). Hence, the formula to calculate the uncertainty is expressed as:

$$\frac{\Delta R_h}{R_h} = \sqrt{\left(\frac{\Delta T_h}{T_h}\right)^2 + \left(\frac{\Delta T_{amb}}{T_{amb}}\right)^2 + \left(\frac{\Delta Q_{in}}{Q_{in}}\right)^2} \tag{13}$$

where

$$\frac{\Delta P_{in}}{P_{in}} = \sqrt{\left(\frac{\Delta V}{V}\right)^2 + \left(\frac{\Delta I}{I}\right)^2 + \left(\frac{\Delta Q_{loss}}{Q_{in}}\right)^2} \tag{14}$$

Table 2 displays the accuracy of the instruments utilized in the experiment. Based on the instrument's accuracy calculations, the uncertainty associated with the measured thermal resistance value discussed in this study is quantified as 2.057%.

5.3. Analysis of experimental results

At an input power of $Q_{in} = 10.08$ W and a heat flux of $q = 700$ W/m^2, the temperature values at each thermocouple monitoring point are recorded. Fig. 20 (a) presents a comparison and validation of the simulation and experimental results for the structure pre- and post-optimization. The figure illustrates that the simulation data aligns

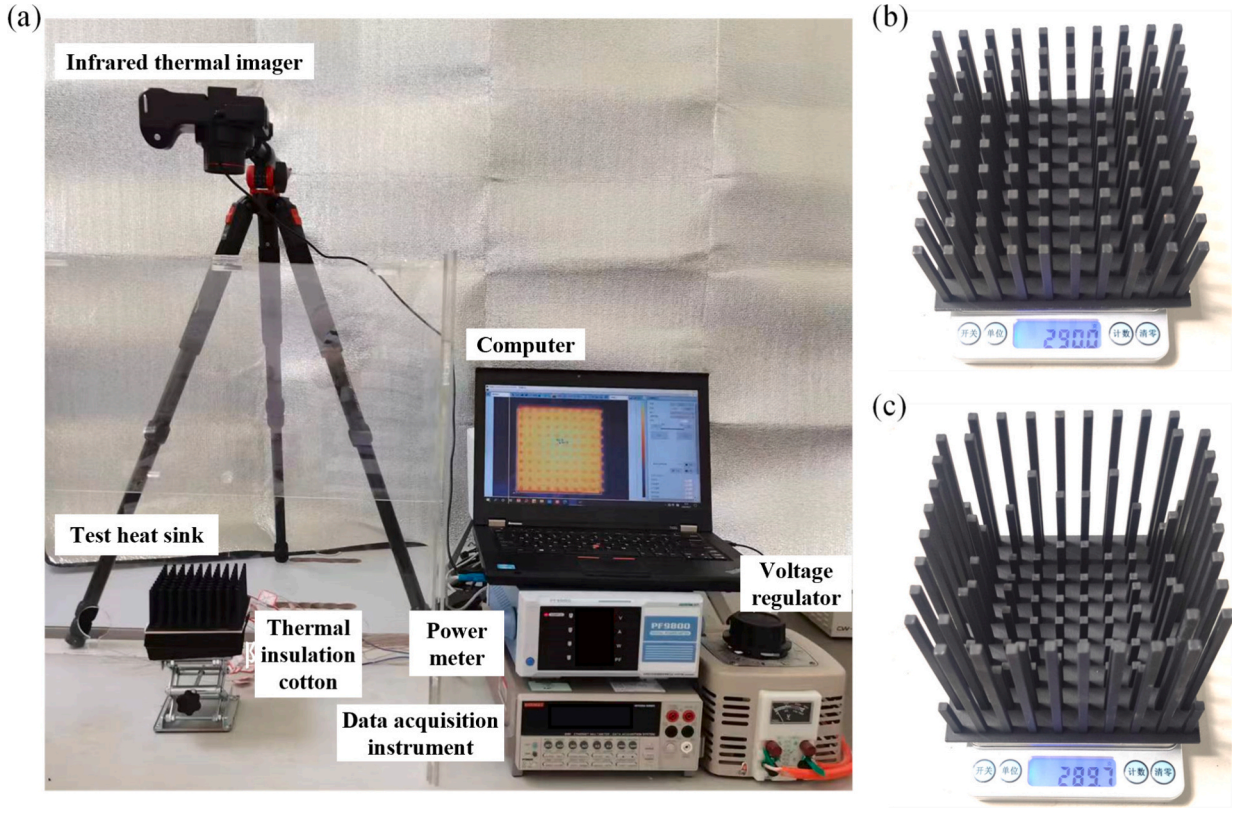

Fig. 18. The experimental bench and heat sink: (a) experimental bench, (b) equal-height pin-fin heat sink, and (c) optimal pin-fin heat sink.

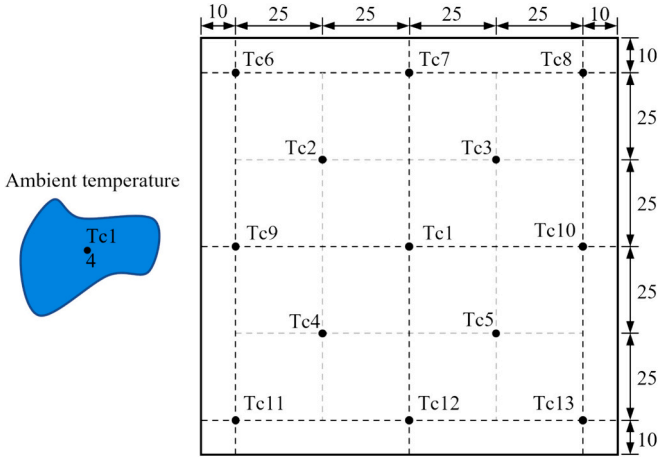

Fig. 19. Distribution diagram of thermocouples.

Table 2
Measuring instruments and accuracy.

instrument	precision
Thermocouple	0.1 K
Data acquisition instrument	0.001 K
Pressure regulator	2%
Power meter	0.01 W

closely with the experimental data, thereby confirming the simulation results' accuracy. Due to heat leakage from the heat source and contact thermal resistance that occur during heat transfer—phenomena not accounted for in the simulation—the experimental values are slightly lower than the simulated ones. Experimental observations also reveal that the post-optimization temperature of the pin-fin heat sink's heating surface is lower than its pre-optimization state, with the temperature differential at the corresponding positions aligning with the simulation results, thus substantiating the optimization's efficacy as modeled dynamically. Fig. 20 (b) depicts the calculated total thermal resistance of the heat sink pre-and post-optimization. The discrepancy between the experimental and simulated values, both pre- and post-optimization, falls within 2%. When considered alongside uncertainty analysis, this discrepancy remains within acceptable limits, affirming the simulation results' validity. The total thermal resistance of the heat sink prior to optimization was R_h = 1.579 K/W, whereas post-optimization, it measured R_h = 1.465 K/W, indicating a reduction of 7.220% in the heat sink's total thermal resistance as determined experimentally.

Furthermore, the surface temperature distributions pre- and post-optimization are analyzed using an infrared imager and contrasted with the simulation results, as depicted in Fig. 21. The infrared imaging findings confirm that the heat sink's surface temperature distribution aligns with the experimental outcomes, further validating the simulation results. Additionally, infrared imaging reveals that the optimized heat sink's surface temperature distribution is lower than its pre-optimized state, suggesting enhanced heat dissipation under identical mass and input power conditions.

The aforementioned analysis indicates that, under a constant input power, the optimized structure demonstrates superior heat dissipation performance according to both experimental and simulation results. To further substantiate the performance comparison of the heat sink pre- and post-optimization at varying power levels, experiments assessing heat dissipation performance are conducted on the structures pre- and post-optimization at various power levels. The input heat flux varied from 500 to 1200 W/m^2, yielding the total thermal resistance distribution for both the heat sinks before and after optimization, as illustrated in Fig. 22. As input power increases, the intensity of natural convection heat transfer and corresponding radiation heat transfer both augment, leading to a decrease in the heat sink's total thermal resistance. Within

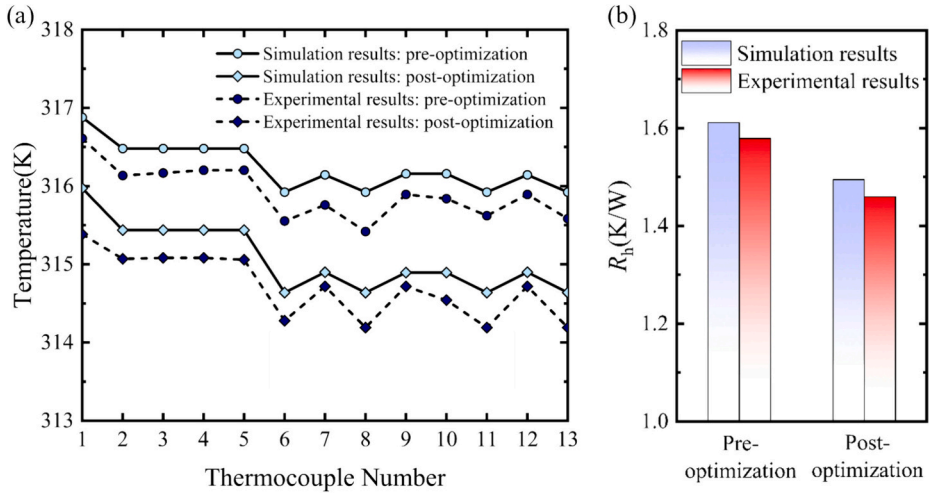

Fig. 20. Comparison of simulation and experimental results when $q = 700$ W/m^2: (a) temperature of thermocouple measuring points and (b) the total thermal resistance of the heat sink.

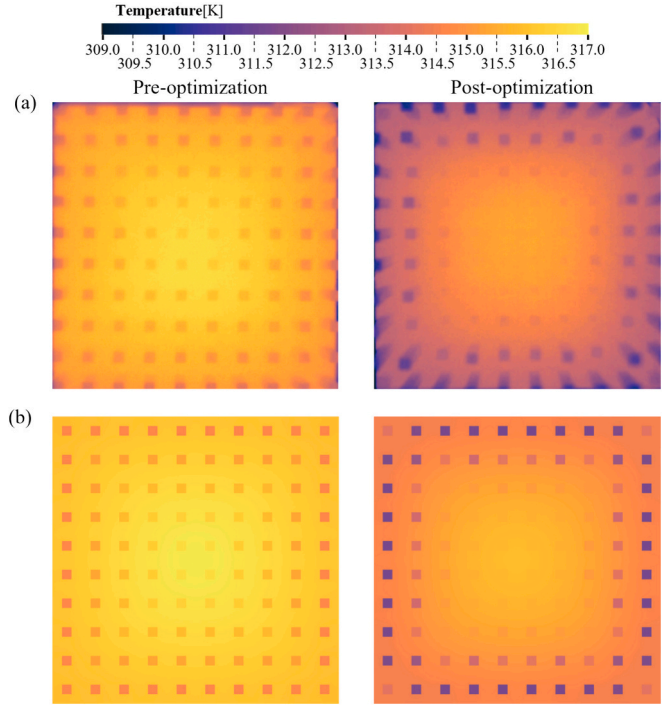

Fig. 21. Heat sink surface temperature distribution: (a) experimental infrared images and (b) numerical simulation results.

the tested range of input power, the optimized structure's total thermal resistance is lower, and its heat dissipation performance surpasses that of the pre-optimized structure at the same mass.

6. Conclusion

In this study, a pin-fin heat sink was chosen to optimize heat transfer efficiency under natural convection. To address the requirements of heat transfer optimization under constrained conditions, an enhanced dynamic surrogate model was developed, and an optimal pin-fin height distribution that does not exceed the original design mass was identified based on the present model. This research elucidates the design principles of pin-fin height distribution in relation to natural convection and confirms the optimization outcomes through experimental validation.

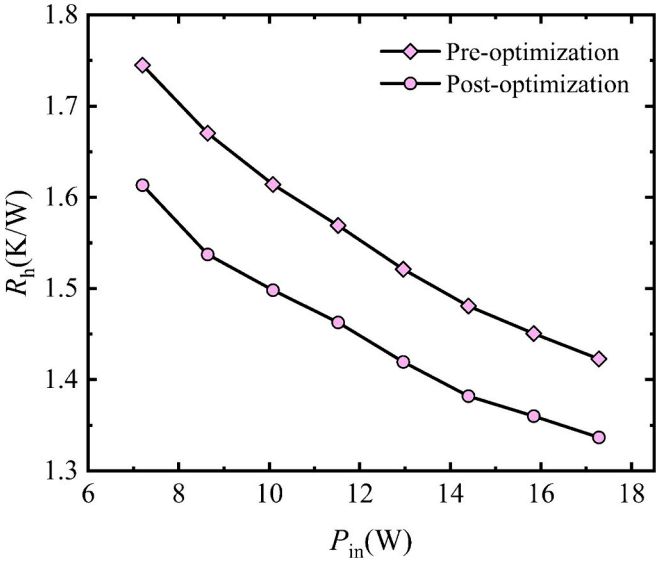

Fig. 22. Total thermal resistance of the structure pre- and post-optimization under different input power.

Some key conclusion can be drawn as follows:

1. Equal-height pin-fin heat sinks exhibit a distribution pattern marked by reduced heat dissipation in the central region and improved dissipation in the peripheral zones. By optimizing the pin-fin height distribution, it is possible to redistribute the heat dissipation and thus improve the heat dissipation performance.
2. A key design principle for pin-fin heat sinks involves elongating fins exhibiting high heat dissipation intensity and truncating those with lower intensity. The optimal configuration exhibits a gradational trend of diminishing pin-fin heights from the periphery towards the center. The thermal resistance of the heat sink, as optimized in this study, shows a reduction of approximately 7%.
3. Optimizing the pin-fin height distribution within the heat sink leads to an enhanced distribution of both the flow and temperature fields, a reduced air flow resistance, an increased mass flux, and a more uniform temperature distribution of the air within the heat sink.
4. The enhancement of thermal dissipation performance in the optimized structure has been confirmed through a comparison between

the numerical and experimental results. The temperature profiles of both the heating surface and the heat sink surface are consistent with those predicted by simulation. Following optimization, thermal resistance decreases with higher power input, and the resulting performance consistently exceeds the pre-optimization state across various power levels.

CRediT authorship contribution statement

Wenhao Fan: Writing – original draft, Visualization, Validation, Software, Methodology, Investigation, Formal analysis, Data curation, Conceptualization. **Chunyu Shi:** Writing – review & editing, Supervision, Methodology, Investigation, Formal analysis. **Wei Liu:** Supervision, Funding acquisition. **Zhichun Liu:** Writing – review & editing, Supervision, Resources, Funding acquisition.

Declaration of competing interest

The authors have declared that no conflict of interest exists.

Data availability

Data will be made available on request.

Acknowledgment

The study is supported by the National Natural Science Foundation of China (No. 52076088) and National Key Research and Development Program of China (No. 2022YFB4003801).

References

[1] S.-W. Chang, A. Sadeghianjahromi, W.-J. Sheu, C.-C. Wang, Numerical study of oblique fins under natural convection with experimental validation, Int. J. Therm. Sci. 179 (2022) 107668, https://doi.org/10.1016/j.ijthermalsci.2022.107668.
[2] C.-H. Huang, W.-Y. Chen, A natural convection horizontal straight-fin heat sink design problem to enhance heat dissipation performance, Int. J. Therm. Sci. 176 (2022) 107540, https://doi.org/10.1016/j.ijthermalsci.2022.107540.
[3] V. Çorumlu, The effects of input power and ambient temperature on the thermal performance of conical pin fin heat sink in natural convection, Int. J. Therm. Sci. 197 (2024) 108855, https://doi.org/10.1016/j.ijthermalsci.2023.108855.
[4] M. Muneeshwaran, M.-K. Tsai, C.-C. Wang, Heat transfer augmentation of natural convection heat sink through notched fin design, International Communications in Heat and Mass Transfer 142 (2023) 106676, https://doi.org/10.1016/j.icheatmasstransfer.2023.106676.
[5] S. Feng, M. Shi, H. Yan, S. Sun, F. Li, T.J. Lu, Natural convection in a cross-fin heat sink, Appl. Therm. Eng. 132 (2018) 30–37, https://doi.org/10.1016/j.applthermaleng.2017.12.049.
[6] S. Siddhartha, S.K. Dash Rath, Thermal performance of a wavy annular finned horizontal cylinder in natural convection for electronic cooling application, International Communications in Heat and Mass Transfer 128 (2021) 105623, https://doi.org/10.1016/j.icheatmasstransfer.2021.105623.
[7] Y. Jiu, H. Fan, W. Wang, Investigation of a novel natural convection heat sink for LEDs based on U-shaped mini-heat pipe arrays, Appl. Therm. Eng. 204 (2022) 118000, https://doi.org/10.1016/j.applthermaleng.2021.118000.
[8] P. Singh, A.K. Patil, Experimental investigation of heat transfer enhancement through embossed fin heat sink under natural convection, Exp. Thermal Fluid Sci. 61 (2015) 24–33, https://doi.org/10.1016/j.expthermflusci.2014.10.011.
[9] W.H. Aldoori, The effect of fin height on forced convection heat transfer from rectangular fin array, Materials Today: Proceedings 80 (2023) 3181–3188, https://doi.org/10.1016/j.matpr.2021.07.191.
[10] C.-H. Huang, Y.-T. Wu, An optimum design for a natural convection pin fin array with orientation consideration, Appl. Therm. Eng. 188 (2021) 116633, https://doi.org/10.1016/j.applthermaleng.2021.116633.
[11] D. Jang, S.-J. Yook, K.-S. Lee, Optimum design of a radial heat sink with a fin-height profile for high-power LED lighting applications, Appl. Energy 116 (2014) 260–268, https://doi.org/10.1016/j.apenergy.2013.11.063.
[12] M. Baldry, V. Timchenko, C. Menictas, Optimal design of a natural convection heat sink for small thermoelectric cooling modules, Appl. Therm. Eng. 160 (2019) 114062, https://doi.org/10.1016/j.applthermaleng.2019.114062.
[13] S.S. Haghighi, H.R. Goshayeshi, M.R. Safaei, Natural convection heat transfer enhancement in new designs of plate-fin based heat sinks, Int. J. Heat Mass Transf. 125 (2018) 640–647, https://doi.org/10.1016/j.ijheatmasstransfer.2018.04.122.
[14] A.A. Sertkaya, M. Ozdemir, E. Canli, Effects of pin fin height, spacing and orientation to natural convection heat transfer for inline pin fin and plate heat sinks by experimental investigation, Int. J. Heat Mass Transf. 177 (2021) 121527, https://doi.org/10.1016/j.ijheatmasstransfer.2021.121527.
[15] G. Sung, D.-Y. Na, S.-J. Yook, Enhancement of the cooling performance of a pin fin heat sink based on the chimney effect using aluminum tape, Int. J. Heat Mass Transf. 201 (2023) 123613, https://doi.org/10.1016/j.ijheatmasstransfer.2022.123613.
[16] D. Kim, D.-K. Kim, Experimental study of natural convection from vertical cylinders with branched pin fins, Int. J. Heat Mass Transf. 177 (2021) 121545, https://doi.org/10.1016/j.ijheatmasstransfer.2021.121545.
[17] Y. Serkan Şahin, B. İsmet Toprak, İ. Solmaz, Ö. Bayer, Investigation of flow and heat transfer behavior of integrated pin fin-aluminum foam heat sink, Appl. Therm. Eng. 219 (2023) 119504, https://doi.org/10.1016/j.applthermaleng.2022.119504.
[18] M. Ahmadian-Elmi, A. Mashayekhi, S.S. Nourazar, K. Vafai, A comprehensive study on parametric optimization of the pin-fin heat sink to improve its thermal and hydraulic characteristics, Int. J. Heat Mass Transf. 180 (2021) 121797, https://doi.org/10.1016/j.ijheatmasstransfer.2021.121797.
[19] P. Bhandari, Y.K. Prajapati, Thermal performance of open microchannel heat sink with variable pin fin height, Int. J. Therm. Sci. 159 (2021) 106609, https://doi.org/10.1016/j.ijthermalsci.2020.106609.
[20] A. Tikadar, S. Kumar, Machine learning approach to predict heat transfer and fluid flow characteristics of integrated pin fin-metal foam heat sink, numerical heat transfer, Part B: Fundamentals (2023) 1–26, https://doi.org/10.1080/10407790.2023.2266772.
[21] M.E. Polat, S. Cadirci, Artificial neural network model and multi-objective optimization of microchannel heat sinks with diamond-shaped pin fins, Int. J. Heat Mass Transf. 194 (2022) 123015, https://doi.org/10.1016/j.ijheatmasstransfer.2022.123015.
[22] K. Kim, H. Lee, M. Kang, G. Lee, K. Jung, C.R. Kharangate, M. Asheghi, K. E. Goodson, H. Lee, A machine learning approach for predicting heat transfer characteristics in micro-pin fin heat sinks, Int. J. Heat Mass Transf. 194 (2022) 123087, https://doi.org/10.1016/j.ijheatmasstransfer.2022.123087.
[23] C. Yu, X. Zhu, Z. Li, Y. Ma, M. Yang, H. Zhang, Optimization of elliptical pin-fin microchannel heat sink based on artificial neural network, Int. J. Heat Mass Transf. 205 (2023) 123928, https://doi.org/10.1016/j.ijheatmasstransfer.2023.123928.
[24] W. Yang, J.K. Mills, Optimization of pin arrangement and geometry in EV and HEV heat sink using genetic algorithm coupled with CFD, in: In: 2021 IEEE International Conference on Mechatronics and Automation (ICMA), IEEE, Takamatsu, Japan, 2021, pp. 332–337, https://doi.org/10.1109/ICMA52036.2021.9512837.
[25] F. Hajabdollahi, H.H. Rafsanjani, Z. Hajabdollahi, Y. Hamidi, Multi-objective optimization of pin fin to determine the optimal fin geometry using genetic algorithm, Appl. Math. Model. 36 (2012) 244–254, https://doi.org/10.1016/j.apm.2011.05.048.
[26] S. Mohsin, A. Maqbool, W.A. Khan, Optimization of cylindrical pin-fin heat sinks using genetic algorithms, IEEE Trans. Comp. Packag. Technol. 32 (2009) 44–52, https://doi.org/10.1109/TCAPT.2008.2004412.
[27] D. Wang, D. Tan, L. Liu, Particle swarm optimization algorithm: an overview, Soft. Comput. 22 (2018) 387–408, https://doi.org/10.1007/s00500-016-2474-6.
[28] V. Maakala, M. Järvinen, V. Vuorinen, Optimizing the heat transfer performance of the recovery boiler superheaters using simulated annealing, surrogate modeling, and computational fluid dynamics, Energy 160 (2018) 361–377, https://doi.org/10.1016/j.energy.2018.07.002.
[29] J. Li, D.J. Jasim, D.H. Kadir, H. Maleki, N.N. Esfahani, M. Shamsborhan, D. Toghraie, Multi-objective optimization of a laterally perforated-finned heat sink with computational fluid dynamics method and statistical modeling using response surface methodology, Eng. Appl. Artif. Intell. 130 (2024) 107674, https://doi.org/10.1016/j.engappai.2023.107674.
[30] H. Towsyfyan, B. Freegah, A.A. Hussain, A.M. El-Deen Faik, Novel design to enhance the thermal performance of plate-fin heat sinks based on CFD and artificial neural networks, Appl. Therm. Eng. 219 (2023) 119408, https://doi.org/10.1016/j.applthermaleng.2022.119408.
[31] R. Baby, C. Balaji, Thermal optimization of PCM based pin fin heat sinks: an experimental study, Appl. Therm. Eng. 54 (2013) 65–77, https://doi.org/10.1016/j.applthermaleng.2012.10.056.
[32] S. Ulaganathan, I. Couckuyt, D. Deschrijver, E. Laermans, T. Dhaene, A Matlab Toolbox for Kriging Metamodelling, Procedia Computer Science 51 (2015) 2708–2713, https://doi.org/10.1016/j.procs.2015.05.395.
[33] H. Lee, G. Lee, K. Kim, D. Kong, H. Lee, Multimodal machine learning for predicting heat transfer characteristics in micro-pin fin heat sinks, Case Studies in Thermal Engineering 57 (2024) 104331, https://doi.org/10.1016/j.csite.2024.104331.
[34] C.-C. Chang, C.-J. Lin, LIBSVM: a library for support vector machines, ACM Trans. Intell. Syst. Technol. 2 (2011) 1–27, https://doi.org/10.1145/1961189.1961199.
[35] D. Das, P. Sharma Abhishek, Application of Taguchi method and response surface methodology (RSM) for parametric optimization of natural convection heat transfer inside a triangular porous enclosure with in-line rectangular finned array, Experimental Heat Transfer (2023) 1–15, https://doi.org/10.1080/08916152.2023.2246974.
[36] M.R. Shaeri, S. Sarabi, A.M. Randriambololona, A. Shadlo, Machine learning-based optimization of air-cooled heat sinks, Thermal Science and Engineering Progress 34 (2022) 101398, https://doi.org/10.1016/j.tsep.2022.101398.
[37] D. Gupta, P. Saha, S. Roy, Multi-objective optimization of air-cooled perforated Micro-pin fin heat sink via an artificial neural network surrogate model coupled with NSGA-II, Journal of Thermal Science and Engineering Applications 16 (2024) 011004, https://doi.org/10.1115/1.4063682.

[38] N.P. Nguyen, E. Maghsoudi, S.N. Roberts, B. Kwon, Shape optimization of pin fin array in a cooling channel using genetic algorithm and machine learning, Int. J. Heat Mass Transf. 202 (2023) 123769, https://doi.org/10.1016/j.ijheatmasstransfer.2022.123769.
[39] L. Yang, Q. Wang, Y. Rao, Searching for irregular pin-fin shapes for high temperature applications using deep learning methods, Int. J. Therm. Sci. 161 (2021) 106746, https://doi.org/10.1016/j.ijthermalsci.2020.106746.
[40] C. Shi, Y. Zhu, M. Yu, Z. Liu, Arrangement optimization of spherical dimples inside tubes based on machine learning for realizing the optimal flow pattern, Thermal Science and Engineering Progress 44 (2023) 102065, https://doi.org/10.1016/j.tsep.2023.102065.
[41] C. Shi, M. Yu, W. Liu, Z. Liu, Shape optimization of corrugated tube using B-spline curve for convective heat transfer enhancement based on machine learning, Sci. China Technol. Sci. 65 (2022) 2734–2750, https://doi.org/10.1007/s11431-022-2088-0.
[42] C. Shi, M. Wang, J. Yang, W. Liu, Z. Liu, Performance analysis and multi-objective optimization for tubes partially filled with gradient porous media, Appl. Therm. Eng. 188 (2021) 116530, https://doi.org/10.1016/j.applthermaleng.2020.116530.
[43] W. Elenbaas, Heat dissipation of parallel plates by free convection, Physica 9 (1942) 1–28, https://doi.org/10.1016/S0031-8914(42)90053-3.
[44] A. Bar-Cohen, W.M. Rohsenow, Thermally optimum spacing of vertical, natural convection cooled, parallel plates, J. Heat Transf. 106 (1984) 116–123, https://doi.org/10.1115/1.3246622.